Observing the Near-Surface Properties of the Greenland Ice Sheet

Scanlan, K. M.; Rutishauser, A.; Simonsen, S. B.

Published in:
Geophysical Research Letters

Link to article, DOI:
10.1029/2022GL101702

Publication date:
2023

Document Version
Publisher's PDF, also known as Version of record

Geophysical Research Letters

RESEARCH LETTER
10.1029/2022GL101702

Observing the Near-Surface Properties of the Greenland Ice Sheet

K. M. Scanlan[1], **A. Rutishauser**[2], **and S. B. Simonsen**[1]

[1]DTU Space, Technical University of Denmark, Kgs. Lyngby, Denmark, [2]Geological Survey of Denmark and Greenland, Copenhagen, Denmark

Key Points:

- In-depth knowledge of near-surface density is crucial for altimetry ice sheet mass balance estimates
- We provide the first, monthly, pan-Greenland observations of surface roughness and density between 2013 and 2018
- Dual-frequency results reflect deposition, melting, and percolation processes through their influence on vertical density heterogeneity

Supporting Information:

Supporting Information may be found in the online version of this article.

Correspondence to:

K. M. Scanlan,
kimis@space.dtu.dk

Citation:

Scanlan, K. M., Rutishauser, A., & Simonsen, S. B. (2023). Observing the near-surface properties of the Greenland ice sheet. *Geophysical Research Letters*, *50*, e2022GL101702. https://doi.org/10.1029/2022GL101702

Received 14 OCT 2022
Accepted 1 MAR 2023

Author Contributions:

Conceptualization: K. M. Scanlan, A. Rutishauser, S. B. Simonsen
Formal analysis: K. M. Scanlan, S. B. Simonsen
Funding acquisition: S. B. Simonsen
Methodology: K. M. Scanlan, A. Rutishauser
Project Administration: K. M. Scanlan, S. B. Simonsen
Software: K. M. Scanlan
Validation: K. M. Scanlan
Visualization: K. M. Scanlan
Writing – original draft: K. M. Scanlan
Writing – review & editing: K. M. Scanlan, A. Rutishauser, S. B. Simonsen

Abstract Spaceborne radar altimetry over ice sheets has exclusively focused on assessing volume changes through changes in surface elevation. For use in mass balance calculations, these measurements are supplemented with surface property information derived from regional climate models with limited large-scale observational validation. Simultaneously, the strength at which a radar signal is reflected from the surface contains information on these same near-surface properties. Here we show that a quantitative interpretation of European (ESA) CryoSat-2 and French/Indian (CNES/ISRO) SARAL surface echo powers yields timeseries of pan-Greenland wavelength-scale roughness and surface density. Individually, the CryoSat-2 and SARAL results strive toward providing an observational lens to enhance our current understanding of the surface processes affecting ice sheet mass balance and validate their representation by computational models. Taken together, they highlight how diversity in currently operational and future radar satellite altimetry missions can shed light on near-surface vertical heterogeneity.

Plain Language Summary For three decades, satellite-based radar altimeters have been measuring areas of thickening and thinning across the Greenland ice sheet (GrIS). From these measurements we can calculate a mass balance, which is an important component in quantifying Greenland's contribution to global mean sea level rise. However, this calculation requires knowing ice sheet surface density. Even though predictable with specialized computer programs, observations are needed to ensure the computer results are accurate. In this study, we use three different radar data sets from two different satellites, to measure the surface density and roughness of the GrIS based on the strength of the radar altimetry surface echoes. As expected, surface roughness increases toward the ice sheet margin and in the vicinity of faster flowing ice. Surface density varies through time and space but appears strongly influenced by melt events (e.g., summer 2012). By comparing measurements between satellites, we can start piecing together how density changes vertically in the near surface; reflecting the processes operating at the time (i.e., snow fall, melting, melt percolation). These observations are the first step toward providing a new data set for refining the computer programs used to project Greenland evolution into the future.

1. Introduction

For three decades, satellite radar altimetry has been accurately measuring surface elevation changes across the Greenland ice sheet (GrIS) (Abdalla et al., 2021; Mottram et al., 2019; Simonsen et al., 2021; The IMBIE Team, 2020). These observations directly feed volumetric mass balance calculations quantifying Greenland's contribution to global sea-level rise (Hurkmans et al., 2014; Khan et al., 2022; McMillan et al., 2016; Mottram et al., 2019; Simonsen et al., 2021; The IMBIE Team, 2020). However, advancements in the use of these data have focused almost exclusively on improving geometric measurements (i.e., the range between the spacecraft and the surface) through either enhanced hardware and acquisition (Le Roy et al., 2007; Phalippou et al., 2001; Rey et al., 2001; Steunou et al., 2015; Verron et al., 2015; Wingham et al., 2006) or post-processing (Gourmelen et al., 2018; Simonsen & Sørensen, 2017; Slater et al., 2019). While often used in corrections to range measurements (Arthern et al., 2001; Simonsen & Sørensen, 2017; Slater et al., 2019), little attention has been paid to the strength of the radar altimetry surface echoes themselves as a direct source of information regarding the GrIS near-surface.

The surface elevation changes derived from satellite radar altimetry require additional information, such as near-surface firn densities and compaction rates, to produce an ice sheet mass balance estimate. However, owing to the harsh nature of the GrIS, there is little opportunity to systematically collect these data in situ (Fausto

et al., 2018). In absence of repeated pan-GrIS observations, model-derived firn conditions support mass balance estimates by (a) providing the density estimates that facilitate the conversion of observed volumetric ice sheet changes to changes in mass and (b) accounting for non-mass loss related changes in surface elevation due to firn densification (Sørensen et al., 2011). Modeled firn conditions (Fausto et al., 2018; Herron & Langway, 1980; Reeh et al., 2005; Zwally & Jun, 2002) rely on possibly tenuous (Fausto et al., 2018) parameterizations against external forcings (e.g., temperature, precipitation, etc.) derived from regional climate models (themselves dependent on local-scale surface roughness estimates (van Tiggelen et al., 2021)) and assumptions regarding firn existence relative to the equilibrium line altitude (Hurkmans et al., 2014; McMillan et al., 2016; Simonsen et al., 2021).

Here we leverage surface echo powers in Ku-band ESA CryoSat-2 (Wingham et al., 2006) and Ka-band CNES/ISRO SARAL (Steunou et al., 2015; Verron et al., 2015) radar waveforms to derive monthly maps of GrIS wavelength-scale surface roughness and density between January 2013 and December 2018. This 6-year period covers contemporaneous CryoSat-2 and SARAL operations before SARAL developed a star tracker issue early in 2019 (Jettou & Rousseau, 2019). Previous research has drawn qualitative relationships between radar altimetry surface echo power and various surface properties (e.g., soil moisture, roughness, vegetation cover) (Fatras et al., 2018; Frappart et al., 2015, 2021; Larue et al., 2021) but stopped short of inverting for the geophysical properties directly. Our approach adopts the Radar Statistical Reconnaissance (RSR) technique developed to study the surface conditions on Mars (Grima et al., 2012) whose outputs are then calibrated using in situ density measurements from the SUMup data set (Montgomery et al., 2018). In addition to Mars, the RSR method has been applied to airborne VHF radar measurements of Antarctica (Grima, Blankenship, et al., 2014; Grima, Schroeder, et al., 2014; Grima et al., 2016, 2019), Devon Ice Cap (Rutishauser et al., 2016), and Ku-band measurements of Saturn's moon Titan (Grima et al., 2017).

2. Materials and Methods

2.1. Radar Altimetry Data Sets

Launched on 8 April 2010, CryoSat-2 and its SIRAL altimeter continue the legacy of Ku-band (13.575 GHz) radar altimetry beginning with ERS-1 in the 1990s (Phalippou et al., 2001; Rey et al., 2001; Wingham et al., 2006). Meanwhile, the ISRO/CNES SARAL spacecraft launched on 25 February 2013, is the first to carry a Ka-band (35.75 GHz) radar altimeter (AltiKa) (Steunou et al., 2015; Verron et al., 2015). SARAL operates with a constant pulse repetition frequency (PRF) of 3.8 kHz and generates stacked waveforms at a rate of 40 Hz (i.e., 25 ms of along-track echo averaging) while CryoSat-2 data acquisition varies with location. In the GrIS interior, CryoSat-2 operates in its Low-Resolution Mode (LRM) with a 1.97 kHz PRF and stacked waveforms generated at a rate of 20 Hz. Over the margins, CryoSat-2 operates in a burst mode, where bursts of 64 pulses (PRF of 18.181 kHz) are measured and then Synthetic Aperture Radar (SAR) processed yielding individual, unfocussed waveforms at a rate of 21 Hz. In addition, a second, cross-track antenna is operated simultaneously to facilitate interferometry. This multi-antenna acquisition mode is referred to as the SAR Interferometric (SARIn) mode. This study makes use of altimetry waveforms contained in the SARAL/ALtiKa Sensor Geophysical Data Record, Baseline-D CryoSat-2 LRM Level 1B (L1B), and Baseline-D CryoSat-2 SIN Full Bit Rate (FBR) data products. Note that the CryoSat-2 SARIn FBR data products are generated prior to SAR focusing and contain all waveforms for each 64-pulse burst for both antennas.

2.2. Surface Echo Power Extraction and Pre-Processing

Surface echo powers are extracted from each waveform individually. For each type of data product, it is assumed that reported power levels are comparable across the observation period (i.e., any data processing or instrument-related effects have been accounted for). The peak surface echo power is defined to be the maximum measured power within a window (5% of the receive window) following the position of the leading edge. The range bin exhibiting the maximum integrated normalized echo amplitude gradient is taken to be representative of that leading edge position. Individual gradients are calculated using the central difference of observed echo amplitudes over three, six, and nine percent of the waveform before being normalized and integrated to identify the maximum. Extracted echo amplitudes are corrected for scaling, atmospheric, and instrument effects using land ice correction factors reported in the SARAL and CryoSat-2 data products.

After extraction, individual surface echo power measurements are either retained or rejected based on the auxiliary information reported in the individual data products. For CryoSat-2 SARIn data products, only measurements not

marked with the internal CAL4 flag are retained. For SARAL, a reported altimetric range more than 1,000 km, a marked trailing edge variation flag, and a large average waveform off-nadir angle (empirically defined as >0.10 degrees-squared) are all used as indicators of poor-quality data points. Finally, extracted surface echo powers are corrected for geometric spreading and variations in the magnitude of the nadir surface slope estimated from the 500 m ArcticDEM (Porter et al., 2018). The slope correction is based on the small angle approximation ($\sin\theta \approx \theta$) and a linear relationship between echo powers expressed in decibels and the logarithm of surface slope for each month (Figure S1 in Supporting Information S1). Echo powers are corrected relative to a slope of 0.1°.

2.3. RSR Application and Quality Control

The RSR method recovers coherent (P_c) and incoherent (P_n) powers by fitting a homodyned K-distribution (HK) to the observed histogram of echo powers (Grima, Blankenship, et al., 2014; Grima, Schroeder, et al., 2014). Following previous studies, 1,000 samples are used to construct the histogram of observed echo powers (Grima, Blankenship, et al., 2014; Grima, Schroeder, et al., 2014; Grima et al., 2016, 2019; Rutishauser et al., 2016). To ensure temporal comparability, for each month the RSR methodology is applied to the 1,000 closest surface echoes surrounding each node of a 5 by 5 km set of grid points (EPSG:3413) spanning the GrIS. While the exact location of individual surface echo measurements will vary month-to-month with the spacecraft orbits, the position of the individual nodes is held constant. It is assumed that surface echo powers are comparable within individual months.

Post calculation of P_c and P_n, all RSR results pass through an additional level of control to again remove low quality data points. Grid nodes where the correlation between the observed echo power histogram and the HK distribution fit is <0.96 (Grima, Blankenship, et al., 2014; Grima, Schroeder, et al., 2014; Grima et al., 2016, 2019; Rutishauser et al., 2016) (Figure S2 in Supporting Information S1) or where one must search more than an empirically determined radial distance (40 km for SARAL, 50 km for CryoSat-2 LRM, and 10 km for CryoSat-2 SIN) (Figure S3 in Supporting Information S1) from the grid node to assemble 1,000 surface echoes have been removed. Final P_c and P_n RSR results for May 2015 are presented as Figures 1a and 1b (SARAL), Figures 1e and 1f (CryoSat-2 LRM), Figures 1i and 1j (CryoSat-2 SARIn).

2.4. Calibration

Calibration shifts the relative, dataset-dependent (SARAL, CryoSat-2 LRM, and CryoSat-2 SARIn) P_c and P_n values to absolute powers that respond directly to changes in surface roughness and density (via the Fresnel reflection coefficient). These calibration values are defined from P_c values near locations where SUMup measurements (Montgomery et al., 2018) reveal a near-surface closely resembling a homogenous firn pack. Specifically, the subset of in situ measurements used in calibration must (a) overlap (in time and space) with the radar altimetry observations and (b) exhibit minimal variations in density within the subsurface depth range the radar altimeters are sensitive to. This depth range is conservatively assumed to be two meters for SARAL and four meters for CryoSat-2 based on estimated penetration depths from Larue et al. (2021). The threshold for a SUMup measurement meeting the homogeneity criterion is a standard deviation in reported densities over the depth range of interest <0.05 g cm^{-3} (Figure S4 in Supporting Information S1). For in situ SUMup measurements that meet these criteria (Figure S5 in Supporting Information S1), the thickness-weighted mean density within the assumed sensitive depth range is compared against the closest P_c value (Figure S6 in Supporting Information S1). A discussion of considerations for a layered near-surface is presented in Section 3.4.

No SUMup measurements meeting the minimal density variability criterion exist near quality-controlled CryoSat-2 SARIn RSR results. Therefore, the CryoSat-2 SARIn calibration value is determined by comparing CryoSat-2 LRM and SARIn P_c results wherever valid values exist for both. Due to CryoSat-2's polar orbit, such grid nodes are found exclusively along the northern boundary between the two acquisition masks. Note that the surface echo powers contributing to the LRM and SARIn RSR results at these grid nodes will be biased to their respective side of the acquisition mask boundary as LRM and SARIn data cannot be acquired simultaneously. A linear relationship is fit between the CryoSat-2 LRM and SARIn P_c results and the slope and intercept of this fit are used to adjust the CryoSat-2 LRM calibration value determined from the in situ data set.

2.5. Backscattering Model and RSR Inversion

Once calibrated, inverting the RSR results for surface density and wavelength-scale roughness requires a backscattering model. Following previous studies, here we assume normal incidence, incoherent backscattering

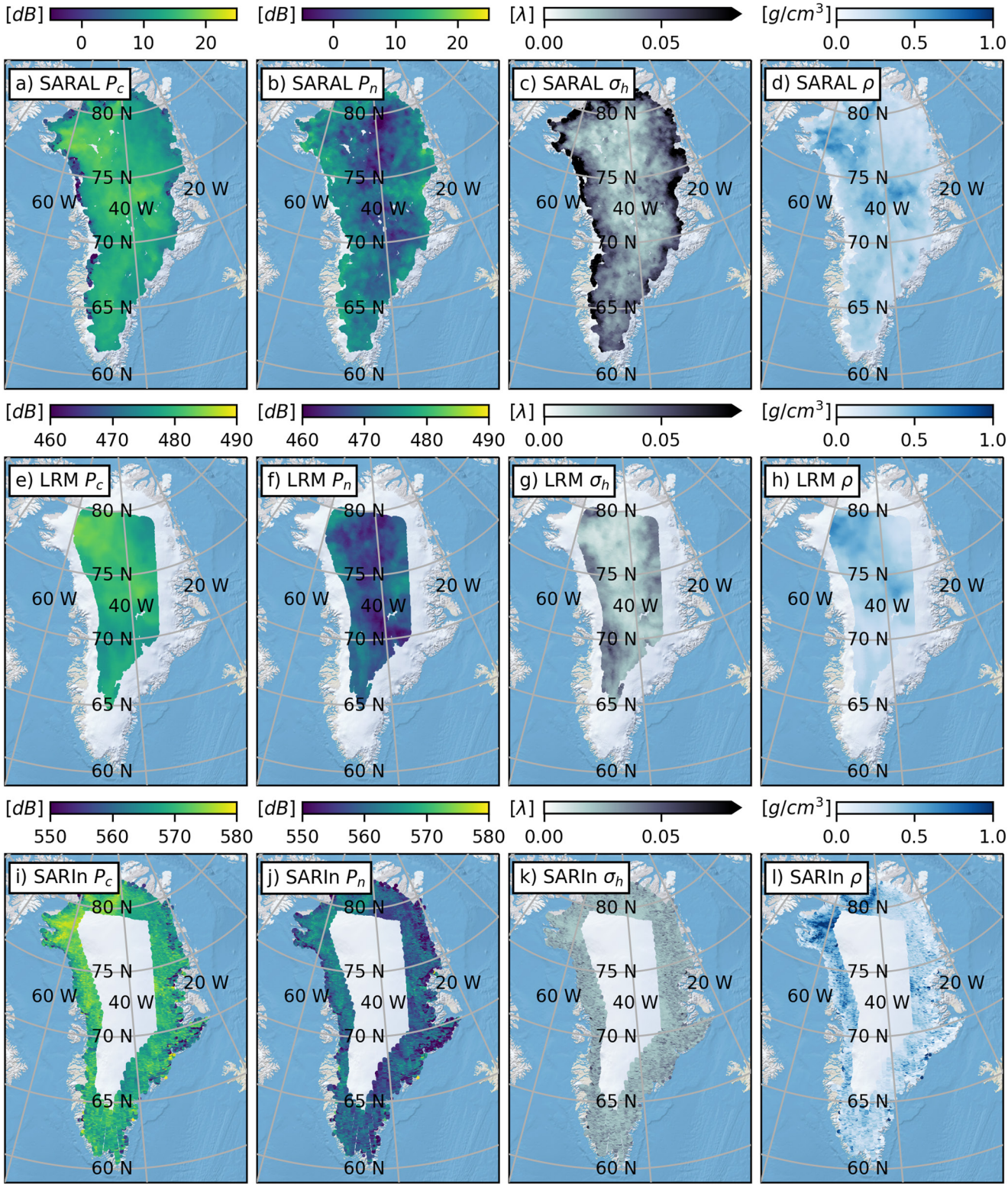

Figure 1. Maps of P_c [(a), (e), and (i)], P_n [(b), (f), and (j)], surface roughness (expressed as fractions of a wavelength) [(c), (g), and (k)] and density [(d), (h), and (l)] derived from the RSR analysis of May 2015 SARAL [(a) through (d)], CryoSat-2 LRM [(e) through (h)] and CryoSat-2 SARIn [(i) through (l)] surface echo powers (larger versions are presented as Figures S8–S11 in Supporting Information S1). There is a clear expression of known features (i.e., NEGIS, outlet glaciers) in the SARAL and CryoSat-2 LRM surface roughness maps. While CryoSat-2 SARIn roughness recovers the smoothest regions, it does not resolve rougher features nearer to the margin. All three data sets reveal density patterns that are consistent in both amplitude and space.

from the GrIS obeys the small perturbation model (SPM) (Grima, Blankenship, et al., 2014; Grima, Schroeder, et al., 2014; Grima et al., 2012; Rutishauser et al., 2016). Intended for radar scattering from slightly rough surfaces, the SPM has a validity range of $k\sigma_h \leq 0.3$ and $kl \leq 3$ where k is the radar wavenumber [m^{-1}], σ_h is the RMS height to the surface [m], and l is the surface roughness correlation length [m]. Implementing the SPM simplifies the derivation of a closed form solution for P_n (Grima et al., 2012). Furthermore, assuming negligible incoherent scattering from titled off-nadir surfaces within the dataset-specific radar footprint, P_c and P_n can be uniquely expressed in terms of surface relative dielectric permittivity (ε_r) and RMS height (Grima, Schroeder, et al., 2014; Grima et al., 2012);

$$P_c = r^2 e^{-(2k\sigma_h)^2}, \text{and} \tag{1}$$

$$P_n = 4k^2 r^2 \sigma_h . \tag{2}$$

The r term in Equation 1 and 2 is the Fresnel reflection coefficient for the surface $\left(\left(1-\sqrt{\varepsilon_r}\right)/\left(1+\sqrt{\varepsilon_r}\right)\right)$. This system of two equations with two unknowns then yields a unique set of geophysical parameters (ε_r and σ_h) for each P_c/P_n combination. The relative dielectric permittivity estimate can be converted to density (ρ) using an empirical model such as

$$\varepsilon_r = 1 + 1.7\rho + 0.7\rho^2 \tag{3}$$

from Pomerleau et al. (2020). This inversion procedure reliably recovers the thickness-weighted in situ densities extracted from the SUMup data set (Montgomery et al., 2018) taken as representative of a homogenous near-surface (Figure S7 in Supporting Information S1). Note that in this context, "surface" refers to the surface as sensed by the radar altimeter (via the reflected waveform), which may be different from the exact boundary between the ice sheet and the atmosphere.

3. Results

3.1. Surface Roughness

Radar altimetry-derived surface roughness for May 2015 are presented as Figures 1c, 1g, and 1k. Spatially, SARAL and CryoSat-2 LRM both reveal a smooth interior becoming progressively rougher toward the margin. Figures 1c and 1g each show a linearly striking region of increased surface roughness in the NE portion of the GrIS (76.4°N/32.4°W) coincident with the inland reaches of the Northeast Greenland Ice Stream (Fahnestock et al., 1993; Solgaard et al., 2021). When displayed on a larger map (Figure 2), the SARAL roughness results also exhibit increased surface roughness associated with the inland reaches of individual glaciers (e.g., 80.0°N/54.0°W and 78.1°N/25.3°W). CryoSat-2 SARIn surface roughness (Figure 1k) does not exhibit the same spatial patterns as the other two radar altimetry data sets (expanded on in Section 3.3). While the smoothest portions of the GrIS persist across the CryoSat-2 LRM/SARIn boundary (e.g., 77.8°N/59.5°W and 79.7°N/38.3°W), the CryoSat-2 SARIn results do not capture known increases in surface roughness toward the ice sheet margin (Porter et al., 2018).

Roughness timeseries at six locations are presented in Figure 2. Note that all six locations fall within the CryoSat-2 LRM operational mask. Location VI is the sole timeseries to suggest the existence of an annual surface roughness cycle; with surface roughness dramatically increasing during the summer in assumed association with surface melting. However, most summer surface roughness estimates have been removed during RSR quality control. The low (<0.96) correlation coefficients are taken to be indicative of an evolving GrIS surface that no longer meets the statistical stability assumptions on which the RSR method is based. This is consistent with the development of melt and flow features (Charalampidis et al., 2016; van Tiggelen et al., 2021) that would locally change how radar signals are reflected from the GrIS during the summer.

All other SARAL timeseries (each north of Location VI) exhibit minimal changes in the mean level of surface roughness across the six-year observation window suggestive of long-term, stable surface conditions. Consistent variabilities in surface roughness around the mean are also observed; with the sole exception being Location I, where SARAL surface roughness variability appears to decrease beginning in 2016. Similar temporal patterns (i.e., consistent mean with consistent variability) also present in the Location II, IV, and V CryoSat-2 timeseries, while Location I is suggestive of a step increase in mean surface roughness after summer 2015 and Location III

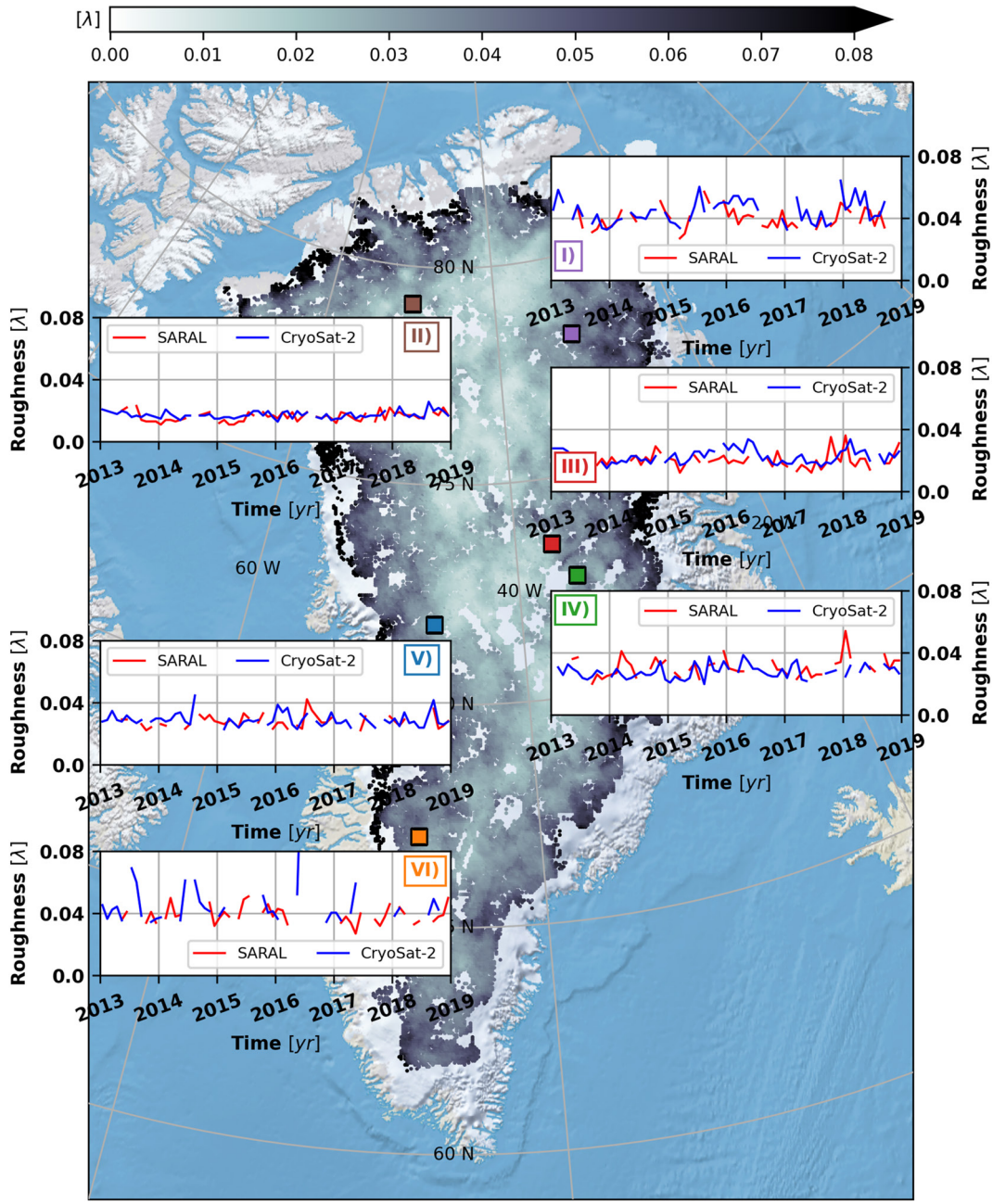

Figure 2. SARAL and CryoSat-2 LRM surface roughness timeseries at six locations across the GrIS overlain on the May 2015 SARAL surface roughness basemap. The timeseries reveal consistent patterns in SARAL and CryoSat-2 LRM surface roughness with only Location VI suggesting the existence of a seasonal cycle.

presents with an apparent slow, low-amplitude multi-year cycle with peaks in winter 2015/2016 and 2017/2018. Recall that the surface roughness results presented in Figures 1 and 2 rely on the assumed backscattering model. Future work will look to validate the application of the SPM for the GrIS surface.

3.2. Surface Density

May 2015 surface density results are presented as Figures 1d, 1h, and 1l. Unlike for surface roughness, the CryoSat-2 SARIn results return density variations comparable to those of the other data sets. Spatially, outside of the western CryoSat-2 LRM/SARIn boundary between 70°N and 76°N, regions of both high (~0.60 g cm^{-3})

and low (~0.25 g cm^{-3}) densities as well as the boundaries between them map consistently across all the observationally derived data sets. The northwest quadrant of the GrIS as well as a quasi-circular region centered at 71.3°N/32.2°W exhibit high near surface densities and surround the low densities observed in the northeast. In the southern half of the GrIS, there is no consistent large-scale pattern in density, but local features do exist and persist across multiple data sets (e.g., SARAL and CryoSat-2 SARIn at 67.6°N/37.0°W and 68.5°N/35.8°W).

The surface density timeseries (Figure 3) present with more temporal and cross-spacecraft variability compared to surface roughness (Figure 2). While each timeseries exhibits elevated densities at the start of 2013, which we speculate as being associated with the extreme pan-GrIS summer 2012 melt event (Houtz et al., 2021; Nghiem et al., 2012), subsequent long-term behavior varies. Locations I (except at the end of 2018), IV, and V each exhibit sustained low densities through time as observed by both the SARAL and CryoSat-2. The Location VI timeseries is difficult to interpret due to temporally sparse results meeting the quality control criterion but generally falls within a similar category as the timeseries of Locations II and III. All three timeseries exhibit periods where the SARAL and CryoSat-2 densities agree and others where the CryoSat-2-derived densities are significantly larger. Location II and III timeseries highlight strong SARAL/CryoSat-2 density differences at the start of the timeseries that have disappeared by the end of 2018, while Location VI exhibits similar SARAL and CryoSat-2 densities in the early portions of the timeseries (2013–2014) followed by marked separations in 2015/2016 and 2017/2018.

3.3. Influence of Data Acquisition

Spatiotemporal patterns in the observed GrIS surface properties (Figures 1–3) contain idiosyncrasies associated with the underlying radar altimetry data sets. The most striking example is spatial resolution; with CryoSat-2 SARIn exhibiting the highest, followed by SARAL and CryoSat-2 LRM. Spatial resolution is related to the radial distance required to collect the 1,000 surface echo powers used to build the statistical echo power distribution (Grima, Schroeder, et al., 2014; Grima et al., 2012). As such, it is a function of both the rate at which data are reported in the individual data products and orbit design. Regarding the latter, as both SARAL and CryoSat-2 follow polar orbits, the spatial density of altimetric measurements naturally increases with latitude as ground tracks converge. For the former, the non-SAR SARAL and CryoSat-2 LRM data products exhibit coarse along-track data rates (40 and 20 Hz, respectively (Phalippou et al., 2001; Rey et al., 2001; Steunou et al., 2015; Verron et al., 2015; Wingham et al., 2006)), which imply broad search radii and the inclusion of surface echoes from multiple orbits when applying the RSR technique. In contrast, the high along-track density pre-SAR focused CryoSat-2 SARIn data (two sets of 21 Hz bursts of 64 pulses with a PRF of 18.181 kHz (Phalippou et al., 2001; Rey et al., 2001; Wingham et al., 2006)) means the 1,000 surface echo powers (or ~8 individual bursts) are often drawn from a single orbit; thereby increasing the spatial resolution. The limitation, however, is that locations with CryoSat-2 SARIn results meeting the quality control requirement related to maximal search radius only occur along or near each orbit groundtrack. As CryoSat-2 groundtracks are not ubiquitous across the GrIS over the course of a month (~1-year groundtrack repeat interval (Wingham et al., 2006)), this introduces coverage gaps in the CryoSat-2 SARIn timeseries (e.g., the southern portion of Figure S10 in Supporting Information S1).

The pre-SAR focusing CryoSat-2 SARIn FBR data also influence the surface roughness estimates (Figure 1k) and its difference compared to those of SARAL and CryoSat-2 LRM (Figures 1c and 1g). Increasing surface roughness corresponds to an increasingly dominant incoherent power (P_n) component (Grima et al., 2012; Grima, Schroeder, et al., 2014). SARAL and CryoSat-2 LRM results (Figures 1a, 1b, 1e, and 1f) demonstrate that while the majority of the GrIS can be considered specular ($P_c > P_n$), P_n becomes more prominent near to the margin. In contrast, the CryoSat-2 SARIn results exhibit an almost constant P_c/P_n difference (Figures 1i and 1j) leading to a more homogeneous surface roughness distribution outside of very smooth regions (Figure 1k). The CryoSat-2 SARIn P_c/P_n mirroring and the excellent agreement between SARAL and CryoSat-2 LRM suggest that the input CryoSat-2 SARIn data are not satisfying an implicit assumption in the RSR methodology; specifically, that related to the statistical independence of the 1,000 surface echo power measurements used in the RSR analysis (Grima, Schroeder, et al., 2014; Grima et al., 2012). For context, the distance between adjacent CryoSat-2 SARIn surface echo power measurements within a single burst is 40 cm (assuming a 7.4 km/s spacecraft speed (Wingham et al., 2006)), and recall that simultaneous measurements from both receive antennas are included. The dominantly specular nature of the GrIS surface limits the influence non-independent spatial sampling has on the CryoSat-2 SARIn surface density results (i.e., Figure 1l) but CryoSat-2 SARIn results closer to the rougher ice sheet margin should be treated with appropriate skepticism. Future work will be directed at how the current RSR implementation can be better adjusted to account for the uniqueness of CryoSat-2 SARIn data.

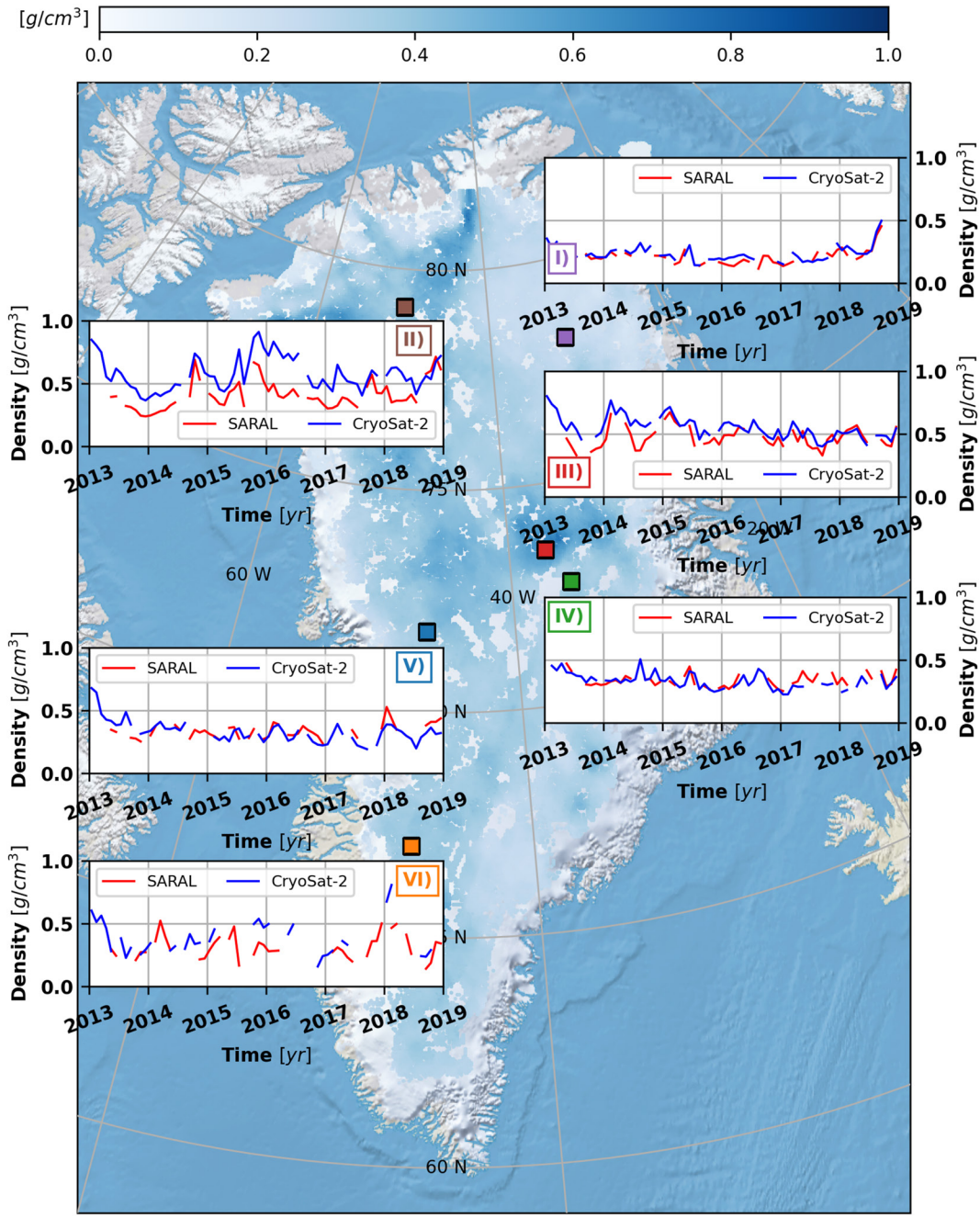

Figure 3. SARAL and CryoSat-2 LRM surface density timeseries at six locations across the GrIS overlain on the May 2015 SARAL density basemap. Differences in SARAL and CryoSat-2 surface densities reflect the interplay between different exciting radar signals and near-surface heterogeneity. CryoSat-2 signals penetrate deeper than SARAL and are therefore more sensitive to deeper subsurface structure. As such, in low accumulation areas, distinct dense layers of refrozen melt will manifest and increase CryoSat-2 observed surface densities for longer than for SARAL.

3.4. Interpreting Density Estimates and Inferring Vertical Heterogeneity

As alluded to in Section 2.5, the surface density results presented in Figures 1 and 3 are a quantitative interpretation of how CryoSat-2 and SARAL radar signals interact with the GrIS near-surface through both space and time. However, this interaction can change depending on how the near-surface responds to climatic forcings. A firn column exhibiting a conventional gradual linear increase in density with depth within the radar-sensitive depth range (Larue et al., 2021), will exhibit similar SARAL and CryoSat-2 surface densities (e.g., Locations I,

IV, and V in Figure 3). As, under these conditions, the strength of the surface echo is dominated by the reflections from the air-snow interface (Grima, Schroeder, et al., 2014). In contrast, a heterogeneous near-surface containing distinct layers (e.g., wind slabs, ice lenses etc. generating sharp permittivity contrasts) will respond differently to different radar altimetry signals depending on how these heterogeneities are organized physically (i.e., their size and position) as well as how that organization changes through time (i.e., downward layer advection with subsequent snowfall).

In the face of a variable near-surface, the different depth sensitivities of CryoSat-2 and SARAL offer a means to infer the existence of near-surface density heterogeneity. For example, Locations II, III and VI (Figure 3) all exhibit CryoSat-2 densities that exceed those of SARAL. This is suggestive of denser material existing at depth to which the deeper-penetrating CryoSat-2 signals are sensitive to but the SARAL signals (at least those contributing to the measured surface echo power) are not. The initially large and progressively diminishing SARAL/CryoSat-2 density differences at Locations II and III suggest a dense layer (i.e., refrozen melt) likely generated following substantial melting in 2012 (Houtz et al., 2021; Nghiem et al., 2012) that is slowly being pushed out of the sensitive depth range due to subsequent ∼4–6 mm of water equivalent [w.e.] (Figure S12 in Supporting Information S1) average annual snowfall (Muñoz Sabater, 2019). Location II is also subject to an additional influx of denser near-surface material possibly associated with melt events in northwest Greenland in 2015 (Houtz et al., 2021; Mousavi et al., 2021). This interplay of accumulation and new melting means it takes approximately 6 years at Location II and 3.5 years at Location III for these dense layers to be pushed out of the CryoSat-2 depth sensitivity range. Once that occurs though, surface densities reflect a smoothly varying near-surface (i.e., equivalent SARAL and CryoSat-2 densities). Dense, near-surface layers are also known to persist through multiple years at Location VI (Charalampidis et al., 2015, 2016). However, they are not clearly represented in the associate timeseries due to large ∼20 mm w.e. average annual snowfall (Muñoz Sabater, 2019), meter-scale percolation depths (Charalampidis et al., 2015, 2016), and rapidly varying summer surfaces that violate the RSR spatial homogeneity assumptions.

Taken together, the comparison of CryoSat-2 and SARAL appears capable of shedding light on vertical density heterogeneities. However, temporal variations in the position of the dominant radar reflecting horizons (in response to new melting and accumulation) imply that the density results cannot be automatically taken as directly representative of true surface densities or densities at a specific depth. Ongoing work is being directed toward developing more absolute means of interpreting the density results such that they can be reliably compared to model predictions and included in future GrIS mass balance estimates.

4. Conclusions

Observations of surface roughness and densities derived from spaceborne radar altimetry measurements represent a new pathway to reducing altimetric ice sheet mass balance estimate dependency on climate models. Hence better constraining the GrIS contribution to global sea-level rise. The spatiotemporal evolution of surface density reflects the balance of melting, percolation, and accumulation processes that modify the near surface on scales relevant to the radar signals being used. As such, these new observations can help assess the performance of computational models used in ice sheet mass balance calculations and improve the reliability of projected ice sheet behavior into the future. Extending further, exciting opportunities exist to refine the satellite-derived assessments of near-surface heterogeneity through the quantitative modeling of radar signal propagation and possible joint interpretations with other remote sensing data sets (e.g., passive microwave). The joint Ku-/Ka-band analysis is also a direct precursor to what might be possible with the next generation of dual frequency satellite radar altimeters such as the European Commission's upcoming Copernicus Polar Ice and Snow Topography Altimeter mission. Overall, the radiometric analysis of spaceborne radar altimetry exploits a previously marginalized aspect of these data to provide new observations directly pertinent to enhancing our understanding of the state of ice sheets.

Data Availability Statement

The quality-controlled RSR data and inverted near-surface property results spanning the Greenland ice sheet between 2013 and 2018 are available through http://data.dtu.dk/ with https://doi.org/10.11583/DTU.21333291.v1.

Acknowledgments
K.M.S. and S.B.S. have been supported by PROTECT. This publication was supported by PROTECT. This project has received funding from the European Union's Horizon 2020 research and innovation programme under Grant agreement No 869304, PROTECT contribution number 60. K.M.S. has also been funded through Villum Fonden (Villum Experiment Programme) Project No. 50225. A.R. has been supported by the Greenland Climate Network (GC-Net) monitoring program. The RSR code has been retrieved from https://github.com/cgrima/rsr (accessed 7 October 2021). SARAL data products are available through the CNES AVISO FTP (ftp-access.aviso.altimetry.fr), while CryoSat-2 data have been downloaded through the ESA CryoSat-2 FTP (science-pds.cryosat.esa.int).

References

Abdalla, S., Abdeh Kolahchi, A., Ablain, M., Adusumilli, S., Aich Bhowmick, S., Alou-Font, E., et al. (2021). Altimetry for the future: Building on 25 years of progress. *Advances in Space Research*, *68*(2), 319–363. https://doi.org/10.1016/j.asr.2021.01.022

Arthern, R. J., Wingham, D. J., & Ridout, A. L. (2001). Controls on ERS altimeter measurements over ice sheets: Footprint-scale topography, backscatter fluctuations, and the dependence of microwave penetration depth on satellite orientation. *Journal of Geophysical Research*, *106*(D24), 33471–33484. https://doi.org/10.1029/2001JD000498

Charalampidis, C., van As, D., Box, J. E., van den Broeke, M. R., Colgan, W. T., Doyle, S. H., et al. (2015). Changing surface–atmosphere energy exchange and refreezing capacity of the lower accumulation area, West Greenland. *The Cryosphere*, *9*(6), 2163–2181. https://doi.org/10.5194/tc-9-2163-2015

Charalampidis, C., Van As, D., Colgan, W. T., Fausto, R. S., Macferrin, M., & Machguth, H. (2016). Thermal tracing of retained meltwater in the lower accumulation area of the southwestern Greenland ice sheet. *Annals of Glaciology*, *57*(72), 1–10. https://doi.org/10.1017/aog.2016.2

Fahnestock, M., Bindschadler, R., Kwok, R., & Jezek, K. (1993). Greenland ice sheet surface properties and ice dynamics from ERS-1 SAR imagery. *Science*, *262*(5139), 1530–1534. https://doi.org/10.1126/science.262.5139.1530

Fatras, C., Borderies, P., Frappart, F., Mougin, E., Blumstein, D., & Niño, F. (2018). Impact of surface soil moisture variations on radar altimetry echoes at Ku and Ka bands in semi-arid areas. *Remote Sensing*, *10*(4), 582. https://doi.org/10.3390/rs10040582

Fausto, R. S., Box, J. E., Vandecrux, B., van As, D., Steffen, K., MacFerrin, M. J., et al. (2018). A snow density dataset for improving surface boundary conditions in Greenland ice sheet firn modeling. *Frontiers of Earth Science*, *6*, 51. https://doi.org/10.3389/feart.2018.00051

Frappart, F., Blarel, F., Papa, F., Prigent, C., Mougin, E., Paillou, P., et al. (2021). Backscattering signatures at Ka, Ku, C and S bands from low resolution radar altimetry over land. *Advances in Space Research*, *68*(2), 989–1012. https://doi.org/10.1016/j.asr.2020.06.043

Frappart, F., Fatras, C., Mougin, E., Marieu, V., Diepkilé, A. T., Blarel, F., & Borderies, P. (2015). Radar altimetry backscattering signatures at Ka, Ku, C, and S bands over West Africa. *Physics and Chemistry of the Earth, Parts A/B/C*, *83–84*, 96–110. https://doi.org/10.1016/j.pce.2015.05.001

Gourmelen, N., Escorihuela, M. J., Shepherd, A., Foresta, L., Muir, A., Garcia-Mondéjar, A., et al. (2018). CryoSat-2 swath interferometric altimetry for mapping ice elevation and elevation change. *Advances in Space Research*, *62*(6), 1226–1242. https://doi.org/10.1016/j.asr.2017.11.014

Grima, C., Blankenship, D. D., Young, D. A., & Schroeder, D. M. (2014). Surface slope control on firn density at Thwaites Glacier, West Antarctica: Results from airborne radar sounding: Surface slope control on firn density. *Geophysical Research Letters*, *41*(19), 6787–6794. https://doi.org/10.1002/2014GL061635

Grima, C., Greenbaum, J. S., Garcia, E. J. L., Soderlund, K. M., Rosales, A., Blankenship, D. D., & Young, D. A. (2016). Radar detection of the brine extent at McMurdo Ice Shelf, Antarctica, and its control by snow accumulation. *Geophysical Research Letters*, *43*(13), 7011–7018. https://doi.org/10.1002/2016GL069524

Grima, C., Koch, I., Greenbaum, J. S., Soderlund, K. M., Blankenship, D. D., Young, D. A., et al. (2019). Surface and basal boundary conditions at the southern McMurdo and Ross ice shelves, Antarctica. *Journal of Glaciology*, *65*(252), 675–688. https://doi.org/10.1017/jog.2019.44

Grima, C., Kofman, W., Herique, A., Orosei, R., & Seu, R. (2012). Quantitative analysis of Mars surface radar reflectivity at 20 MHz. *Icarus*, *220*(1), 84–99. https://doi.org/10.1016/j.icarus.2012.04.017

Grima, C., Mastrogiuseppe, M., Hayes, A. G., Wall, S. D., Lorenz, R. D., Hofgartner, J. D., et al. (2017). Surface roughness of Titan's hydrocarbon seas. *Earth and Planetary Science Letters*, *474*, 20–24. https://doi.org/10.1016/j.epsl.2017.06.007

Grima, C., Schroeder, D. M., Blankenship, D. D., & Young, D. A. (2014). Planetary landing-zone reconnaissance using ice-penetrating radar data: Concept validation in Antarctica. *Planetary and Space Science*, *103*, 191–204. https://doi.org/10.1016/j.pss.2014.07.018

Herron, M., & Langway, C., Jr. (1980). Firn densification: An empirical model. *Journal of Glaciology*, *25*(93), 373–385. https://doi.org/10.3189/S0022143000015239

Houtz, D., Mätzler, C., Naderpour, R., Schwank, M., & Steffen, K. (2021). Quantifying surface melt and liquid water on the Greenland ice sheet using L-band radiometry. *Remote Sensing of Environment*, *256*, 112341. https://doi.org/10.1016/j.rse.2021.112341

Hurkmans, R. T. W. L., Bamber, J. L., Davis, C. H., Joughin, I. R., Khvorostovsky, K. S., Smith, B. S., & Schoen, N. (2014). Time-evolving mass loss of the Greenland ice sheet from satellite altimetry. *The Cryosphere*, *8*(5), 1725–1740. https://doi.org/10.5194/tc-8-1725-2014

Jettou, G., & Rousseau, M. (2019). SARAL/Altika validation and cross calibration activities Annual report 2019 (No. SALP-RP-MA-EA-23419-CLS) (p. 102). Collecte Localisation Satellites. Retrieved from https://www.aviso.altimetry.fr/fileadmin/user_upload/SALP-RP-MA-EA-23419-CLS_AnnualReport_SARAL_2019.pdf

Khan, S. A., Bamber, J. L., Rignot, E., Helm, V., Aschwanden, A., Holland, D. M., et al. (2022). Greenland mass trends from airborne and satellite altimetry during 2011–2020. *Journal of Geophysical Research: Earth Surface*, *127*(4), e2021JF006505. https://doi.org/10.1029/2021JF006505

Larue, F., Picard, G., Aublanc, J., Arnaud, L., Robledano-Perez, A., LE Meur, E., et al. (2021). Radar altimeter waveform simulations in Antarctica with the Snow Microwave Radiative Transfer Model (SMRT). *Remote Sensing of Environment*, *263*, 112534. https://doi.org/10.1016/j.rse.2021.112534

Le Roy, Y., Deschaux-Beaume, M., Mavrocordatos, C., Aguirre, M., & Heliere, F. (2007). SRAL SAR radar altimeter for sentinel-3 mission. In *2007 IEEE international geoscience and remote sensing symposium* (pp. 219–222). IEEE. https://doi.org/10.1109/IGARSS.2007.4422769

McMillan, M., Leeson, A., Shepherd, A., Briggs, K., Armitage, T. W. K., Hogg, A., et al. (2016). A high-resolution record of Greenland mass balance. *Geophysical Research Letters*, *43*(13), 7002–7010. https://doi.org/10.1002/2016gl069666

Montgomery, L., Koenig, L., & Alexander, P. (2018). The SUMup data set: Compiled measurements of surface mass balance components over ice sheets and sea ice with analysis over Greenland. *Earth System Science Data*, *10*(4), 1959–1985. https://doi.org/10.5194/essd-10-1959-2018

Mottram, R., Simonsen, S. B., Høyer Svendsen, S., Barletta, V. R., Sandberg Sørensen, L., Nagler, T., et al. (2019). An integrated view of Greenland ice sheet mass changes based on models and satellite observations. *Remote Sensing*, *11*(12), 1407. https://doi.org/10.3390/rs11121407

Mousavi, M., Colliander, A., Miller, J. Z., Entekhabi, D., Johnson, J. T., Shuman, C. A., et al. (2021). Evaluation of surface melt on the Greenland ice sheet using SMAP *L*-band microwave radiometry. *IEEE Journal of Selected Topics in Applied Earth Observations and Remote Sensing*, *14*, 11439–11449. https://doi.org/10.1109/JSTARS.2021.3124229

Muñoz Sabater, J. (2019). ERA5-land monthly averaged data from 1981 to present. *Copernicus Climate Change Service (C3S) Climate Data Store (CDS)*. https://doi.org/10.24381/cds.68d2bb3

Nghiem, S. V., Hall, D. K., Mote, T. L., Tedesco, M., Albert, M. R., Keegan, K., et al. (2012). The extreme melt across the Greenland ice sheet in 2012. *Geophysical Research Letters*, *39*(20), 2012GL053611. https://doi.org/10.1029/2012GL053611

Phalippou, L., Rey, L., & de Chateau-Thierry, P. (2001). Overview of the performances and tracking design of the SIRAL altimeter for the CryoSat mission. In *IGARSS 2001. Scanning the present and resolving the future. Proceedings. IEEE 2001 international geoscience and remote sensing symposium (Cat. No.01CH37217)* (Vol. 5, pp. 2025–2027). IEEE. https://doi.org/10.1109/IGARSS.2001.977891

Pomerleau, P., Royer, A., Langlois, A., Cliche, P., Courtemanche, B., Madore, J.-B., et al. (2020). Low cost and compact FMCW 24 GHz radar applications for snowpack and ice thickness measurements. *Sensors*, *20*(14), 3909. https://doi.org/10.3390/s20143909

Porter, C., Morin, P., Howat, I., Noh, M.-J., Bates, B., Peterman, K., et al. (2018). ArcticDEM. Harvard dataverse. https://doi.org/10.7910/DVN/OHHUKH

Reeh, N., Fisher, D. A., Koerner, R. M., & Clausen, H. B. (2005). An empirical firn-densification model comprising ice lenses. *Annals of Glaciology*, *42*, 101–106. https://doi.org/10.3189/172756405781812871

Rey, L., de Chateau-Thierry, P., Phalippou, L., Mavrocordatos, C., & Francis, R. (2001). SIRAL, a high spatial resolution radar altimeter for the Cryosat mission. In *IGARSS 2001. Scanning the present and resolving the future. Proceedings. IEEE 2001 international geoscience and remote sensing symposium (Cat. No.01CH37217)* (Vol. 7, pp. 3080–3082). IEEE. https://doi.org/10.1109/IGARSS.2001.978261

Rutishauser, A., Grima, C., Sharp, M., Blankenship, D. D., Young, D. A., Cawkwell, F., & Dowdeswell, J. A. (2016). Characterizing near-surface firn using the scattered signal component of the glacier surface return from airborne radio-echo sounding. *Geophysical Research Letters*, *43*(24), 12502–12510. https://doi.org/10.1002/2016GL071230

Simonsen, S. B., Barletta, V. R., Colgan, W. T., & Sørensen, L. S. (2021). Greenland ice sheet mass balance (1992–2020) from calibrated radar altimetry. *Geophysical Research Letters*, *48*(3), e2020GL091216. https://doi.org/10.1029/2020GL091216

Simonsen, S. B., & Sørensen, L. S. (2017). Implications of changing scattering properties on Greenland ice sheet volume change from Cryosat-2 altimetry. *Remote Sensing of Environment*, *190*, 207–216. https://doi.org/10.1016/j.rse.2016.12.012

Slater, T., Shepherd, A., Mcmillan, M., Armitage, T. W. K., Otosaka, I., & Arthern, R. J. (2019). Compensating changes in the penetration depth of pulse-limited radar altimetry over the Greenland ice sheet. *IEEE Transactions on Geoscience and Remote Sensing*, *57*(12), 9633–9642. https://doi.org/10.1109/TGRS.2019.2928232

Solgaard, A., Kusk, A., Merryman Boncori, J. P., Dall, J., Mankoff, K. D., Ahlstrøm, A. P., et al. (2021). Greenland ice velocity maps from the PROMICE project. *Earth System Science Data*, *13*(7), 3491–3512. https://doi.org/10.5194/essd-13-3491-2021

Sørensen, L. S., Simonsen, S. B., Nielsen, K., Lucas-Picher, P., Spada, G., Adalgeirsdottir, G., et al. (2011). Mass balance of the Greenland ice sheet (2003–2008) from ICESat data—The impact of interpolation, sampling and firn density. *The Cryosphere*, *5*(1), 173–186. https://doi.org/10.5194/tc-5-173-2011

Steunou, N., Desjonquères, J. D., Picot, N., Sengenes, P., Noubel, J., & Poisson, J. C. (2015). AltiKa altimeter: Instrument description and in flight performance. *Marine Geodesy*, *38*(sup1), 22–42. https://doi.org/10.1080/01490419.2014.988835

The IMBIE Team. (2020). Mass balance of the Greenland ice sheet from 1992 to 2018. *Nature*, *579*(7798), 233–239. https://doi.org/10.1038/s41586-019-1855-2

van Tiggelen, M., Smeets, P. C. J. P., Reijmer, C. H., Wouters, B., Steiner, J. F., Nieuwstraten, E. J., et al. (2021). Mapping the aerodynamic roughness of the Greenland ice sheet surface using ICESat-2: Evaluation over the K-transect. *The Cryosphere*, *15*(6), 2601–2621. https://doi.org/10.5194/tc-15-2601-2021

Verron, J., Sengenes, P., Lambin, J., Noubel, J., Steunou, N., Guillot, A., et al. (2015). The SARAL/AltiKa altimetry satellite mission. *Marine Geodesy*, *38*(sup1), 2–21. https://doi.org/10.1080/01490419.2014.1000471

Wingham, D. J., Francis, C. R., Baker, S., Bouzinac, C., Brockley, D., Cullen, R., et al. (2006). CryoSat: A mission to determine the fluctuations in Earth's land and marine ice fields. *Advances in Space Research*, *37*(4), 841–871. https://doi.org/10.1016/j.asr.2005.07.027

Zwally, H. J., & Jun, L. (2002). Seasonal and interannual variations of firn densification and ice-sheet surface elevation at the Greenland summit. *Journal of Glaciology*, *48*(161), 199–207. https://doi.org/10.3189/172756502781831403